Journal of Biomedical Optics

BiomedicalOptics.SPIEDigitalLibrary.org

Functionalized erythrocyte-derived optical nanoparticles to target ephrin-B2 ligands

Taylor Hanley
Rong Yin
Jenny T. Mac
Wenbin Tan
Bahman Anvari

SPIE.

Taylor Hanley, Rong Yin, Jenny T. Mac, Wenbin Tan, Bahman Anvari, "Functionalized erythrocyte-derived optical nanoparticles to target ephrin-B2 ligands," *J. Biomed. Opt.* **24**(8), 085002 (2019), doi: 10.1117/1.JBO.24.8.085002.

Journal of Biomedical Optics 24(8), 085002 (August 2019)

Functionalized erythrocyte-derived optical nanoparticles to target ephrin-B2 ligands

Taylor Hanley,[a] Rong Yin,[b] Jenny T. Mac,[c] Wenbin Tan,[b,*] and Bahman Anvari[a,*]
[a]University of California, Riverside, Department of Bioengineering, Riverside, California, United States
[b]University of South Carolina School of Medicine, Department of Cell Biology and Anatomy, Columbia, South Carolina, United States
[c]University of California, Riverside, Department of Biochemistry, Riverside, California, United States

Abstract. Over- or under-expression of erythropoietin-production human hepatocellular receptors (Eph) and their ligands are associated with various diseases. Therefore, these molecular biomarkers can potentially be used as binding targets for the delivery of therapeutic and/or imaging agents to cells characterized by such irregular expressions. We have engineered nanoparticles derived from erythrocytes and doped with the near-infrared (NIR) FDA-approved dye, indocyanine green. We refer to these nanoparticles as NIR erythrocyte-derived transducers (NETs). We functionalized the NETs with the ligand-binding domain of a particular Eph receptor, EphB1, to target the genetically modified human dermal microvascular endothelial cells (hDMVECs) with coexpression of EphB1 receptor and its ligand ephrin-B2. This cell model mimics the pathological phenotypes of lesional endothelial cells (ECs) in port wine stains (PWSs). Our quantitative fluorescence imaging results demonstrate that such functionalized NETs bind to the ephrin-B2 ligands on these hDMVECs in a dose-dependent manner that varies sigmoidally with the number density of the particles. These nanoparticles may potentially serve as agents to target PWS lesional ECs and other diseases characterized with over-expression of Eph receptors or their associated ligands to mediate phototherapy. [DOI: 10.1117/1.JBO.24.8.085002]

Keywords: Eph receptors; nanomaterials; near infrared fluorescence imaging; port wine stains; red blood cells.

Paper 190033R received Feb. 10, 2019; accepted for publication Jul. 29, 2019; published online Aug. 19, 2019.

1 Introduction

Erythropoietin-production human hepatocellular (Eph) receptors are the most abundant subgroup of receptor tyrosine kinases, with at least 16 different members being expressed in humans.[1] These receptors are divided into two subclasses based largely on their binding affinities for the two subclasses of ephrin ligands (ephrin-A or ephrin-B), and are referred to as EphA or EphB receptors.[1–5] EphA receptors tend to bind ephrin-A ligands; while EphB receptors preferentially bind to ephrin-B ligands.[1–5] These receptors and ligands are involved in a number of physiological processes involving the development of the nervous system, angiogenesis, and cell migration.[3,4,6,7]

Over- or under-expression of Eph receptors and their ligands have been associated with lung, breast, and prostate cancers, as well as melanomas and leukemia.[8] Some Eph receptors and ephrins have also been reported to play a role in bone homeostasis and implicated in myeloma bone disease, osteolytic bone disease associated with breast cancer metastasis,[9] and skeletal deformities including cleft palates and craniosynostosis.[10] Deregulation of Eph receptor and ephrin ligand signaling has also been implicated in aberrant synaptic functions associated with neurodegenerative diseases such as Alzheimer's disease.[11] Recently, we found that EphB1 receptors and ephrin-B2 ligands are coexpressed on the lesional endothelial cells (ECs) in patients with port wine stains (PWSs).[12]

Due to their abundance on a variety of cell types, Eph receptors and their ligands have become viable targets for therapeutic agents that can be conjugated to various targeting moieties including peptides, antibodies, and the ephrins themselves.[13–20] For example, Blevins et al.[15] conjugated a peptide that targets EphA2 and EphA4 to a PEG linker and a polymer for the delivery of therapeutic plasmids to the pancreas. Targeting the Eph/ephrin system has also been done by attaching the targeting agent to a variety of nanoparticles. For example, various targeting agents have been conjugated to hollow gold nanospheres, gold-coated silica nanoshells, biosynthesized magnetite nanoparticles, liposomal nanoparticles, and gold nanorods.[14,16–19] In addition to delivering therapeutics, some nanoparticles can deliver imaging and photodynamic therapy agents to specific cells.[13,14,20]

Recently, use of cells such as erythrocytes or nanoparticles coated with cell membranes as therapeutic or imaging platforms has drawn increased attention.[21–31] A particular feature of erythrocytes that distinguishes them from other cell types is their naturally long circulation time (≈90 to 120 days) attributed to the presence of "self-marker" proteins on their surface to inhibit the immune response.[32,33] One putative self-marker is CD47 glycoprotein, which impedes phagocytosis through signaling with phagocytes receptor, SIRPα.[34–37] Hence, constructs derived from erythrocytes may provide their cargo available in circulation for prolonged times.[38] For example, Hu et al. reported that polymeric nanoconstructs coated with erythrocyte-derived membranes were retained in mouse blood for 3 days with a circulation half-life of ≈8 h.[21] As constructs that can be engineered autologously (or from similar blood types), erythrocyte-derived particles also present a potentially nontoxic and biocompatible delivery platform.

We provided the first report of erythrocyte-derived nanoparticles doped with the FDA-approved near-infrared (NIR) dye, indocyanine green (ICG).[22] We refer to these constructs as

*Address correspondence to Wenbin Tan, E-mail: wenbin.tan@uscmed.sc.edu; Bahman Anvari, E-mail: anvarib@ucr.edu

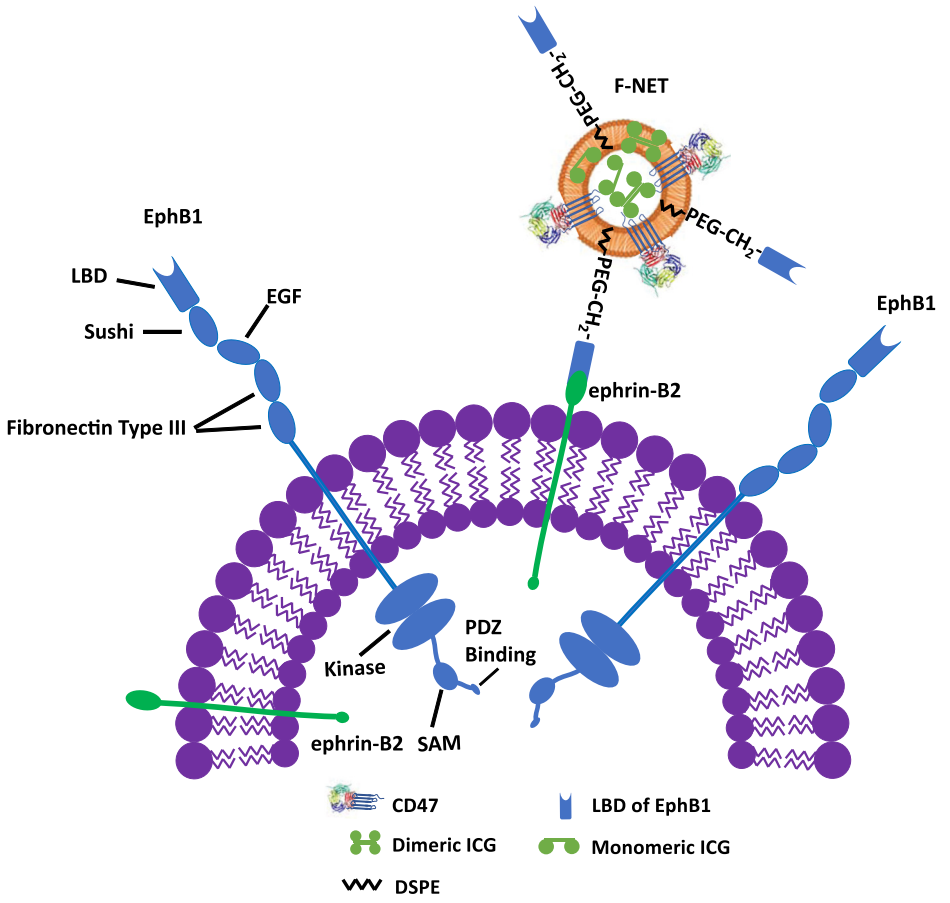

Fig. 1 Schematic of a PWS EC that coexpresses the EphB1 receptor and ephrin-B2 ligand. F-NETs are functionalized with the LBD of EphB1 to selectively bind to ephrin-B2.

NIR erythrocyte-derived transducers (NETs) since, once photoexcited by an appropriate NIR wavelength, ICG can transduce the absorbed light energy to emit fluorescence, generate heat, or mediate the production of reactive oxygen species.[39] We have previously demonstrated the effectiveness of antibody-functionalized NETs in targeted imaging of ovarian cancer cells, as well as NETs functionalized with tissue plasminogen activator as a theranostic agent for NIR fluorescence imaging and thrombolysis of blood clots *in vitro*.[23,24]

Herein we report for the first time the engineering of NETs functionalized with the ligand binding domain (LBD) of the EphB1 receptor (Fig. 1). We chose the LBD of the EphB1 receptor as the targeting agent since it has a strong binding affinity for the ephrin-B2 ligand.[3] We demonstrate the effectiveness of such functionalized NETs (F-NETs) in targeting ECs that overexpress the ephrin-B2 ligand by fluorescence imaging. These optical constructs can potentially be useful to target the ephrin-B2 ligand on a variety of diseases ranging from cancer cells to PWS ECs.

2 Materials and Methods

2.1 *Fabrication of NETs and F-NETs*

Erythrocytes were isolated from either bovine or human whole blood (Rockland Immunochemicals, Inc. and Innovative Research, Inc., respectively) via centrifugation ($1000 \times g$ for 5 to 10 min at 4°C). The plasma and buffy coat were removed, and the erythrocyte pellet was resuspended in ≈320 mOsm phosphate buffered saline (PBS) (defined as $1 \times$PBS). Erythrocytes were centrifuged ($1000 \times g$ for 5 to 10 min at 4°C) and washed with $1 \times$PBS three times with the supernatant discarded after each wash. The erythrocyte pellet was then subjected to hypotonic treatment by resuspension in $0.25 \times$ PBS (≈80 mOsm) for ≈10 min followed by centrifugation ($20{,}000 \times g$ for 20 min at 4°C). The supernatant containing hemoglobin was discarded, and the hypotonic treatment was repeated until the erythrocyte pellet was opaque, indicating the formation of erythrocyte ghosts (EGs).

To form nonfunctionalized NETs, EGs were extruded sequentially through 400- and 200-nm polycarbonate porous membranes (VWR, Inc.) using an Avanti mini extruder (Avanti Polar Lipids, Inc.), resulting in nano-sized EGs (nEGs). These nEGs were then suspended in a solution made of equal volumes of $1 \times$PBS, 0.1 M Sϕrenson's buffer (Na_2HPO_4/NaH_2PO_4, 140 mOsm, pH ≈ 8), and ICG solution (Fisher Scientific Company). Concentration of ICG in the loading buffer solution was either 25 or 33.33 μM, depending on the experiment. The solution was then centrifuged (≈$56{,}000 \times g$ for 1 h at 4°C) and the supernatant was removed. The pellet, comprised of NETs, was then resuspended in $1 \times$PBS, centrifuged, and washed two times. NETs were resuspended in $1 \times$PBS for experiments.

To fabricate F-NETs, we proceeded as follows. EGs (as prepared above) were centrifuged ($20{,}000 \times g$ for 15 min at 4°C) and the supernatant was discarded (Fig. 2). We made a solution

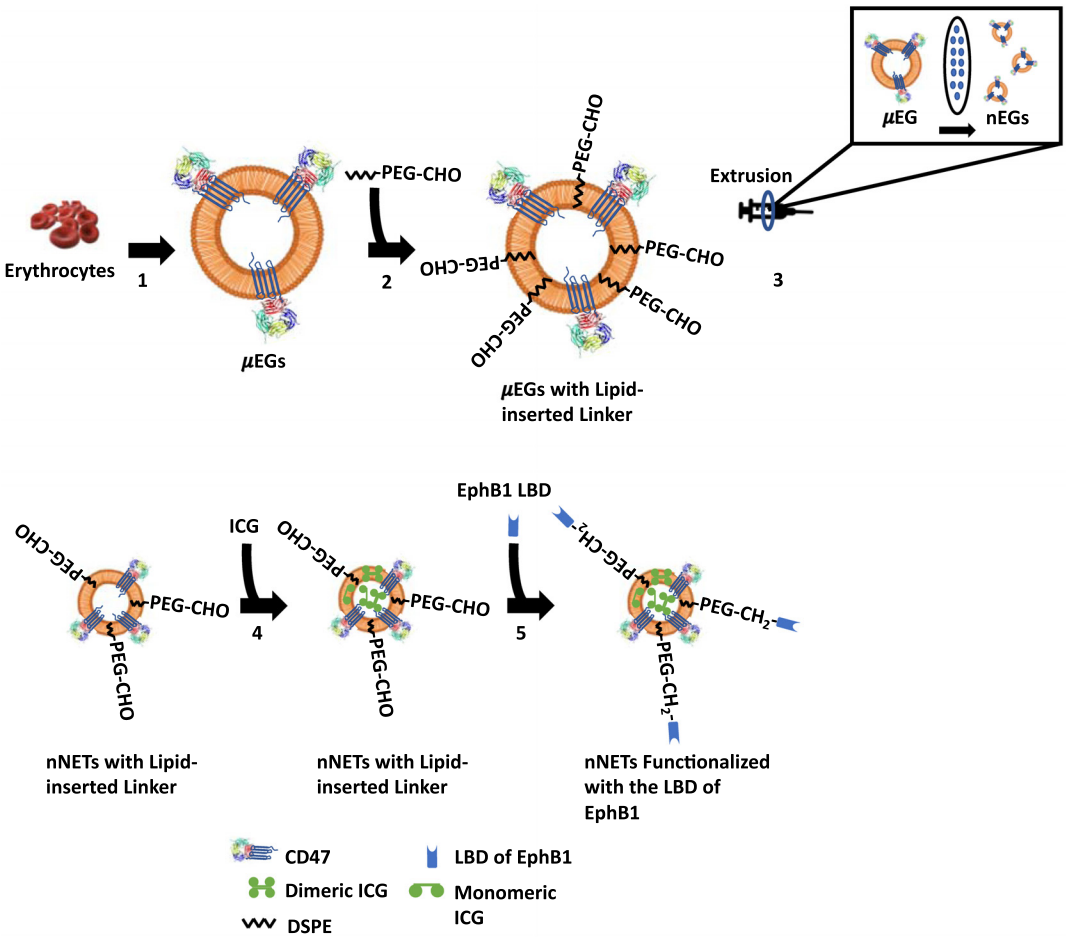

Fig. 2 Schematic of steps to fabricate F-NETs. (1) EGs were formed by depleting the hemoglobin content of erythrocytes. (2) EGs were incubated with a DSPE-PEG-CHO linker for insertion into the lipid phase of EG's shell. (3) Micron-sized EGs (μEGs) with lipid-inserted linkers were extruded to make linker bearing nano-sized EGs (nEGs). A zoomed-in cross-section of the extruder filters with nano-sized pores for extrusion of μEGs into nEGs is shown. (4) nEGs with lipid-inserted linkers were loaded with ICG in a hypotonic solution resulting in formation of nano-sized NETs containing lipid-inserted linkers. (5) The EphB1 LBD was covalently attached to the terminal end of lipid-inserted linkers using a reductive amination reaction to functionalize the NETs. For illustration purposes, we also show one of the erythrocyte membrane proteins, CD47.

consisting of 5 mg of a linker, 1,2-distearoyl-sn-glycero-3-phosphoethanolamine-polyethylene glycol-aldehyde (DSPE-PEG-CHO) (2000 Da PEG) (Nanocs, Inc.) dissolved in 1 ml nanopure water. We added 20 μl of this lipid linker solution to 1 ml of EGs in nanopore water and let the solution incubate (30 min at room temperature). The resulting lipid-inserted EGs were then filtered through 50k Amicon Ultra-4 centrifuge filter units (Millipore) via centrifugation ($\approx$1700 $\times$ g for 10 to 15 min at room temperature) to remove excess linker. As excess lipid-linker and nanopore water were removed through the filter units, the lipid-inserted EGs remained suspended in solution by replenishing with 1 $\times$ PBS. Lipid-inserted EGs were then extruded, and then loaded with either 25 or 33.33 μM ICG in the loading buffer (as described above). The resulting NETs with lipid-inserted linker were resuspended in 1 $\times$ PBS and incubated with 10 μg/ml recombinant Rat EphB1 Fc Chimera Protein, Cf (R&D Systems, Inc.) (hereafter referred to as the EphB1 LBD) for 5 min at room temperature in the dark. This chimera protein is composed of the extracellular LBD of rat EphB1, a short polypeptide sequence, and human IgG_1. We added 5 μl of 20-mM sodium dithionite, as the reducing agent, to the solution containing the NETs with lipid-inserted linkers, and incubated for 1 h at 4°C in the dark. The amine group on the C-terminus end of the EphB1 LBD protein serves as the site for covalent coupling with the aldehyde group on the end of the lipid linker, induced by reductive amination reaction. During this reaction, the Schiff base formed at the site of covalent coupling is reduced by the sodium dithionite, irreversibly converting the imine to a more stable amine. This reaction results in covalent attachment of the EphB1 LBD to NETs. The resulting pellet, comprised of F-NETs, was then washed in 1 $\times$ PBS and centrifuged as described above before being resuspended in 1 $\times$ PBS (Fig. 2).

2.2 *Dynamic Light Scattering-Based Measurements of Particle Diameters*

Hydrodynamic diameters of NETs and F-NETs suspended in 1 $\times$ PBS were measured by dynamic light scattering (DLS) (Zetasizer Nanoseries, NanoZS90, Malvern Instruments). All measurements were made with the particle suspensions in

polystyrene cuvettes with a 1-cm pathlength. Measurements were collected three times for each sample and averaged to calculate the mean diameter and standard deviation (SD) for each population sample. The percentage of each sample's population associated with a given diameter was plotted, and data were fit with a Lognormal function using Igor.

2.3 *Absorption and Fluorescence Spectra of NETs and F-NETs*

Absorption spectra of NETs and F-NETs suspended in $1\times$ PBS were recorded in the 280- to 1000-nm spectral range using a UV visible spectrophotometer (Cary 50 UV-Vis spectrophotometer, Agilent Technologies) with an optical path length of 1 cm. Both NETs and F-NETs were fabricated using 25 μM ICG in the loading buffer. Suspensions of NETs or F-NETs, diluted to have absorbance values of one at 800 nm, were designated to have the relative number density (N^*) of 1× when suspended in $1\times$ PBS. To obtain solutions with a lower N^*, the nanoparticle solutions were diluted by increasing the volume of $1\times$ PBS as desired. To obtain solutions with a higher N^*, the nanoparticle solutions were concentrated using less $1\times$ PBS as desired. We prepared solutions of NETs and F-NETs with N^* ranging from 0.25× (lowest relative number density of nanoparticles) to 2× (highest relative number density of nanoparticles) for various experiments.

Fluorescence spectra of NETs and F-Nets suspended in $1\times$ PBS in response to photoexcitation at 720 ± 2.5 nm with a 450-W xenon lamp were acquired using a fluorometer (Fluorolog-3 spectrofluorometer, Edison). We normalized the wavelength (λ)-dependent fluorescence emission $\chi(\lambda)$ as follows:

$$\chi(\lambda)=\frac{F(\lambda)}{1-10^{-A(\lambda_{ex})}}, \tag{1}$$

where F is the fluorescence emission intensity in response to photo-excitation at a given λ, and $A(\lambda_{ex})$ is the absorbance of the sample at the excitation wavelength. For this characterization, both sets of NETs and F-NETs were fabricated using 33.33 μM ICG in the loading buffer.

2.4 *Functionalization Validation*

We validated the functionalization of NETs with the LBD of the EphB1 receptor by using immunofluorescent staining. Specifically, NETs (control) and F-NETs were fabricated using 33.33 μM ICG in the loading buffer and incubated with 10 μl human IgG Fc Phycoerythrin (PE)-conjugated antibodies (R&D Systems, Inc.) per 1 ml of NETs or F-NETs solution for 1 h at room temperature in the dark. These antibodies bind to the human IgG_1 portion of the EphB1 LBD. Nanoparticles were centrifuged and washed in 1× PBS three times and then photoexcited at 488 ± 2.5 nm (450-W xenon lamp) to elicit emission from the PE. The resulting fluorescence emission spectra were recorded and normalized as described above.

2.5 *Human Dermal Microvascular Endothelial Cell Culture and Transfection*

Human dermal microvascular endothelial cells (hDMVECs) were cultured in endothelial cell basal medium (ECBM) with growth supplement (Cell Applications, Inc.) as previously described.[12] In order to establish the EC models with coexpression of EphB1 receptors and ephrin-B2 ligands, which mimic the pathological phenotypes of PWS ECs, we isolated a subset of normal hDMVECs with high expression of surface EphB1 receptors via biotinylated chimera ephrin-B2-Fc, which contains the extracellular portion of ephrin-B2 ligands and is capable of binding to EphB1 receptors, and streptavidin-conjugated magnetic beads. The rationale of this selection is that the ephrin-B2-Fc chimera ligand binds to $EphB1^+/EphB4^+$ expressing venous and capillary hDMVEC subpopulation, while the remaining arterial hDMVEC subpopulation ($EphB1^-/EphB4^-$) express ephrin-B2 ligands.

Specifically, 100 μg of the streptavidin-conjugated magnetic beads were incubated with 2 μg of biotinylated chimera ephrin-B2 Fc at room temperature for 15 min before the ephrin-B2 Fc-magnetic bead complex was removed from solution via magnetic strands. The bead complex was then incubated with $\approx5\times10^5$ hDMVECs on ice for 30 min. The cells that bound to the bead complex were isolated and designated as $EphB1^+$/ephrin-$B2^-$ hDMVECs, which have previously been verified to express the EphB1 receptor, with undetectable ephrin-B2 levels.[12]

Lentiviral vector pLX304-EphrinB2 containing human ephrin-B2 cDNA was obtained from DNASU (Clone ID: HsCD00446022). Control lentiviral vector pLIM1-EGFP (enhanced green fluorescent protein) was obtained from Addgene (Plasmid ID: 19319). The third-generation lentiviral packaging plasmids were used to produce pLX304-EphrinB2 and pLIM1-EGFP lentiviruses in Phoenix cells. The ephrin-B2 selected hDMVEC subpopulation showed a higher level of EphB1 mRNA and a much lower level of ephrin-B2 mRNA as compared to nonselected heterogeneous hDMVEC populations.[12] $EphB1^+$/ephrin-$B2^-$ hDMVECs were infected by either lentiviruses containing EGFP ($EGFP^+/EphB1^+$/ephrin-B^{2-} hDMVECs) (referred to as control cells) or human EphrinB2 cDNA to overexpress ephrin-B2 ($EphB1^+$/ephrin-$B2^+$ hDMVECs) (referred to as ephrin-B2 cells). The cells were continuously cultured for 2 weeks to allow the expression of transgenes for the F-NETs experiments. The ephrin-B2 expression in the hDMVECs was determined by Western blot assay, as we previously described. Beta-actin was used as the internal loading control.[12]

2.6 *Targeting Ephrin-B2 Ligands by F-NETs*

To determine the effectiveness of the F-NETs to target the ephrin-B2 ligand, we incubated the control and ephrin-B2 cells with either NETs or F-NETs for 40 min at 4°C in the dark. The incubating solution consisted of 50% human ECBM containing 10% fetal bovine serum (FBS) by volume, with the nanoparticles in $1\times$ PBS forming the other 50%. Both NETs and F-NETs were fabricated using 33.33 μM ICG in the loading buffer solution. The relative number density of the particles ($\rho*$) in $1\times$ PBS and ECBM with 10% FBS cell media was defined as

$$\rho*=\frac{N^*\,V_{\text{nanoparticles}}}{V_{\text{nanoparticles}}+V_{\text{ECMB}}}, \tag{2}$$

where $V_{\text{nanoparticle}}$ is the volume of NETs or F-NETs suspension in $1\times$ PBS, and V_{ECBM} is the volume of ECBM and 10% FBS. Cells were incubated with NETs having $\rho*$ of 0.5×, and F-NETs with $\rho*$ values ranging from 0.03× to 0.5×.

After incubation, cells were stained with 500 μl of 4',6-diamidino-2-phenylindole (DAPI) (10 to 11 μM) for subsequent

fluorescence microscopy imaging experiments. DAPI fluorescence emission in response to photo-emission at 360 ± 20 nm by a xenon/mercury arc lamp (Nikon Eclipse Ti-S microscope with an Osram Sylvania XBO75W/2 bulb, Interlight) was captured by an electron multiplier gained CCD camera (Quant EM-CCD, C9100-14 Hamamatsu) over the spectral band of 435 to 485 nm. NIR fluorescence emission (>770 nm), emanating from ICG in NETs, was captured in response to photoexcitation at 740 ± 35 nm. We present falsely colored fluorescent images associated with DAPI-stained nuclei (blue channel) and ICG emission (red channel).

2.7 *Image Analysis*

Acquired NIR fluorescent images of the cells were analyzed using ImageJ software. Regions of interests (ROIs) were selected on a given image. The mean intensity $\overline{I}$ value from a given set of ROIs was calculated as

$$\overline{I} = \frac{\sum_{l=1}^{m}\left[\sum_{k=1}^{n}\left(\frac{\sum_{j=1}^{p} I_j^{\mathrm{ROI}} - I_j^{\mathrm{Background}}}{p}\right)\right]}{m * n}, \tag{3}$$

where I_j^{ROI} is the fluorescence emission intensity at the j'th pixel in the ROI of a given image, $I_j^{\mathrm{background}}$ is the fluorescence emission intensity corresponding to the background region of the same image, p is the total number of pixels in a given ROI, n is the number of ROIs, and m is the number of images obtained from the cell population. Multiple ROIs were selected from a given image, and multiple images from a cell population were used to calculate $\overline{I}$ for each population of cells.

3 Results and Discussion

3.1 *Hydrodynamic Diameter Distribution of NETs and F-NETs*

As determined by fitting lognormal distributions to DLS-based measurements, the average hydrodynamic diameters $\pm$ SD of nonfunctionalized NETs and F-NETs were 127.96 ± 1.58 and 156.76 ± 2.52 nm, respectively (Fig. 3). Our previously published transmission electron and scanning electron microscopic images of NETs have shown that DLS-based measurements of NETs diameter are consistent with those obtained by electron microscopy.[22,23] The increase in the mean diameter of F-NETs by ≈28.8 nm suggests that the thickness of the linker and the LBD coated onto the F-NETs was ≈14.4 nm. Minelli and Shard[40] measured the thickness of 2-kDa thiol terminated methoxy PEG coatings on gold nanoparticles to range from ≈3 to 16 nm. The DPSE-PEG-CHO linker used in our functionalization of NETs has a similar structure to the linker used by Minelli and Shard. Therefore, our estimate of the coating thickness is reasonable and consistent with this previous literature.

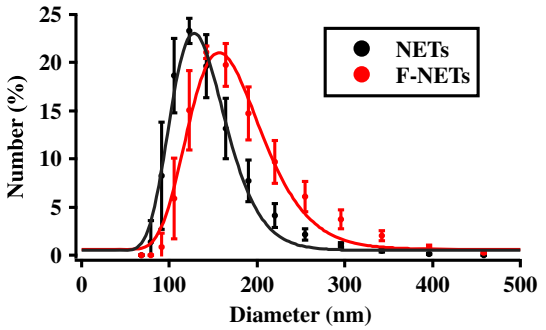

Fig. 3 Hydrodynamic diameters of NETs and F-NETs suspensions. Suspensions were in PBS and the hydrodynamic diameters were measured by DLS. We present the average (circles) with SD values (error bars) associated with three measurements of a sample. Lognormal distributions are fitted to the measured data (solid traces). Black data points and traces correspond to the NETs population, while the red data points and traces correspond to the F-NETs population.

3.2 *Absorption and Fluorescence Spectra of NETs and F-NETs*

Absorption spectra of NETs and F-NETs suspensions in $1 \times$ PBS as a function of N^* of the particles are shown in Figs. 4(a) and 4(b), respectively. Absorption at ≈795 and ≈735 nm corresponds to the monomeric and H-like aggregate forms of ICG, respectively.[22,41,42] There was a near linear relationship between the absorbance values at 795 nm and N^*. For example, when N^* was increased to 2×, the absorbance value at 795 nm increased from ≈1.0 to ≈1.8 for both sets of nanoparticles. The similar absorbance values at 795 nm for NETs and F-NETs for all N^* values suggests that the loading efficiency of ICG was the same for both sets of nanoparticles.

There was a similar near-linear relationship between the absorbance values at 280 nm, the wavelength associated with the protein absorption[43] of NETs, and N^*. For example, when N^* was increased to 2×, the absorbance value at 280 nm increased from ≈0.8 to ≈1.4 for both sets of nanoparticles. For the same N^*, there were minimal differences between the absorbance values at 280 nm for NETs and F-NETs. This result suggests that for a given N^*, the population of F-NETs and NETs had the same amount of proteins, and the EphB1 LBD did not contribute to the absorbance of F-NETs at 280 nm.

In response to photoexcitation at 720 ± 2.5 nm, NETs and F-NETs produced nearly identical fluorescence emission spectra in the 735- to 900-nm band [Fig. 5(a)], associated with the monomer form of ICG.[42] Successful functionalization of NETs with the EphB1 LBD was evidenced by the drastically different fluorescence emission spectrum of F-NETs over the 550- to 630-nm spectral band, in response to 488 ± 2.5 nm photoexcitation, as compared to that of the NETs [Fig. 5(b)]. This band is associated with the fluorescence emission of the phycoerythrin (PE) dye[44,45] that was conjugated to the antibodies that bind to the human IgG_1 part of the EphB1 LBD. The emission spectra provide evidence toward successful functionalization of the F-NETs with the EphB1 LBD [Fig. 5(b)], while at the same

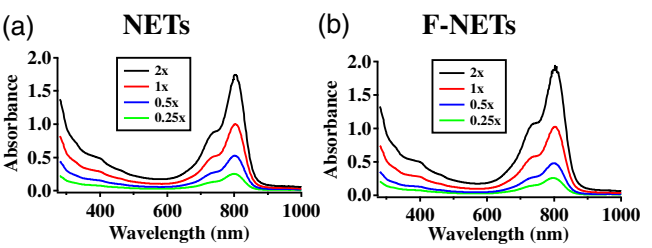

Fig. 4 Absorption spectra of NETs and F-NETs. Absorption spectra of: (a) NETs and (b) F-NETs recorded in $1 \times$ PBS for various values of N^* ranging between 0.25 and 2×. Both NETs and F-NETs were fabricated using 25 μM ICG in the loading buffer.

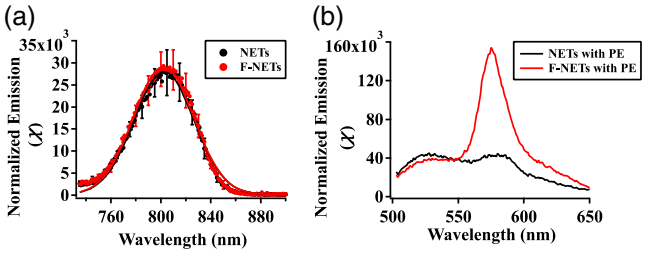

Fig. 5 Normalized fluorescence emission spectra of NETs and F-NETs. (a) Normalized fluorescence emission spectra of NETs and F-NETs in response to photo-excitation at 720 ± 2.5 nm. We present the average (circles) with SD values (error bars) associated with four samples. Gaussian functions fit the data (solid traces). (b) Normalized fluorescence emission spectra of non-functionalized NETs and F-NETs after incubation with human PE-labeled IgG Fc antibodies in response to photoexcitation at 488 ± 2.5 nm. All spectral recordings were made with the particles suspended in $1 \times$ PBS and $N^* = 1\times$. Both NETs and F-NETs were fabricated with 33.33 μM ICG in the loading buffer.

time demonstrating that the NIR emission characteristics of F-NETs remained unaltered as compared to that of NETs [Fig. 5(a)].

3.3 *Targeting Ephrin-B2 Ligands by F-NETs*

We verified the expression of ephrin-B2 on hDMVECs using a Western blot (Fig. 6). Even when incubated with NETs at the highest $\rho*$ value (0.5×), there was minimal NIR fluorescence emission from the control and ephrin-B2 hDMVECs (image not shown), suggesting that nonfunctionalized NETs were not effectively uptaken by either cell type. We quantified the average NIR emission ($\bar{I}$) using Eq. (3). There were no statistically significant differences among $\bar{I}$ values for control hDMVECs whether incubated with NETs or F-NETs with $\rho*$ value of 0.5× (data not shown), suggesting that both particles were uptaken at about the same levels by the control hDMVECs. These results further suggest that the interaction of control hDMVECs with either NETs or F-NETs is likely due to nonspecific binding, with uptake of the particles by clathrin-mediated endocytosis or caveolae-dependent endocytosis.[46]

There was also minimal NIR fluorescence emission from control hDMVECs after incubation with F-NETs, regardless of the $\rho*$ value investigated (images not shown). This result

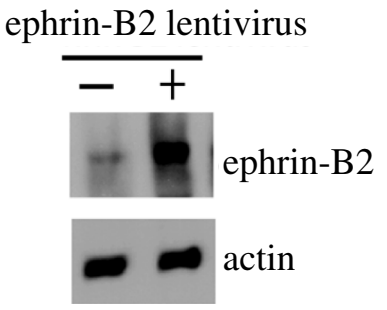

Fig. 6 Ephrin-B2 Western blot expression. Western blot showing the expression of ephrin-B2 in hDMVECs infected with an ephrin-B2 lentivirus compared to the ephrin-B2 expression level of hDMVECs not infected with the ephrin-B2 lentivirus. Beta-actin levels are shown as the internal loading control.

suggests that F-NETs were not effective in targeting hDMVECs that lacked the ephrin-B2 ligand. NIR emission from the ephrin-B2 hDMVECs emerged when the $\rho*$ value for F-NETs exceeded 0.12×, suggesting that there was a threshold number density of F-NETs for effective targeted imaging of ephrin-B2 hDMVECs [Fig. 7(a)].

As the $\rho*$ value of F-NETs increased from 0.03× to 0.5×, there was no clear trend in $\bar{I}$ values for control hDMVECs [Fig. 7(b)]. There were also no statistically significant differences in $\bar{I}$ values associated with control and ephrin-B2 hDMVECs when the $\rho*$ value of F-NETs was 0.03× or 0.06×. However, for $\rho^* \geq 0.12\times$ there were statistically significant differences ($p < 0.001$) between the $\bar{I}$ values associated with the control and ephrin-B2 hDMVECs. Specifically, for ephrin-B2 cells, there was a sigmoidal relationship between the $\bar{I}$ values and ρ^* value of F-NETs [Fig. 7(c)]. This result suggests that a threshold number density of F-NETs ($\rho^* = 0.12\times$) was needed to overcome nonspecific binding between F-NETs and ephrin-B2 hDMVECs. Once those nonspecific binding sites were saturated, excessive F-NETs occupied almost all the available specific EphB1 LBD positions on the ephrin-B2 hDMVECs.

A particular application of F-NETs relates to laser treatment of cutaneous capillary malformations, PWSs. PWSs are currently treated by laser irradiation using visible wavelengths in the range of 585 to 595 nm. These wavelengths target the endogenous hemoglobin to induce photothermal destruction of the PWS vasculatures.[47] However, the melanin pigment within the melanocytes, located in the basal epidermal layer of skin and residing over the abnormal plexus of dermal blood vessels, has relatively strong optical absorption over the current laser treatment band. For example, at treatment wavelength of 585 nm, the absorption coefficient of a melanosome is comparable to that of oxyhemoglobin.[48] As such, the photons intended to reach the dermal vasculature would be partially absorbed within the epidermis. The outcome is nonspecific thermal injury to the epidermis and insufficient heat generation within the vasculatures, leading to an inadequate treatment.

An alternative phototherapeutic approach can potentially be developed by using NIR wavelengths in conjunction with intravascular administration of F-NETs. For example, by changing the treatment wavelength from 585 to 755 nm, nearly threefold reduction in the absorption coefficient of a single melanosome can be achieved.[48] This approach offers several advantages: (1) reduced risk of nonspecific thermal injury to the epidermis to potentially allow treatment of individuals with moderate to heavy pigmentation;[49] (2) increased depth of optical penetration to reach deeply seated blood vessels (e.g., >500 μm below the skin surface);[49] (3) targeted delivery of F-NETs to the ECs within the PWS vasculature where the ephrin-B2 ligand is over-expressed;[12] and (4) heat generation within the blood vessels resulting from the absorption of ICG within the F-NETs to induce photothermal destruction of the lesional vasculature plexus.

4 Conclusions

To the best of our knowledge, we have demonstrated for the first time the fabrication of erythrocyte-derived nanoparticles containing ICG, and functionalized with the EphB1 LBD to target cells that express ephrin-B2. Optical absorption and fluorescence characteristics of NETs remain unaltered upon functionalization with EphB1 LBD. Our quantitative imaging

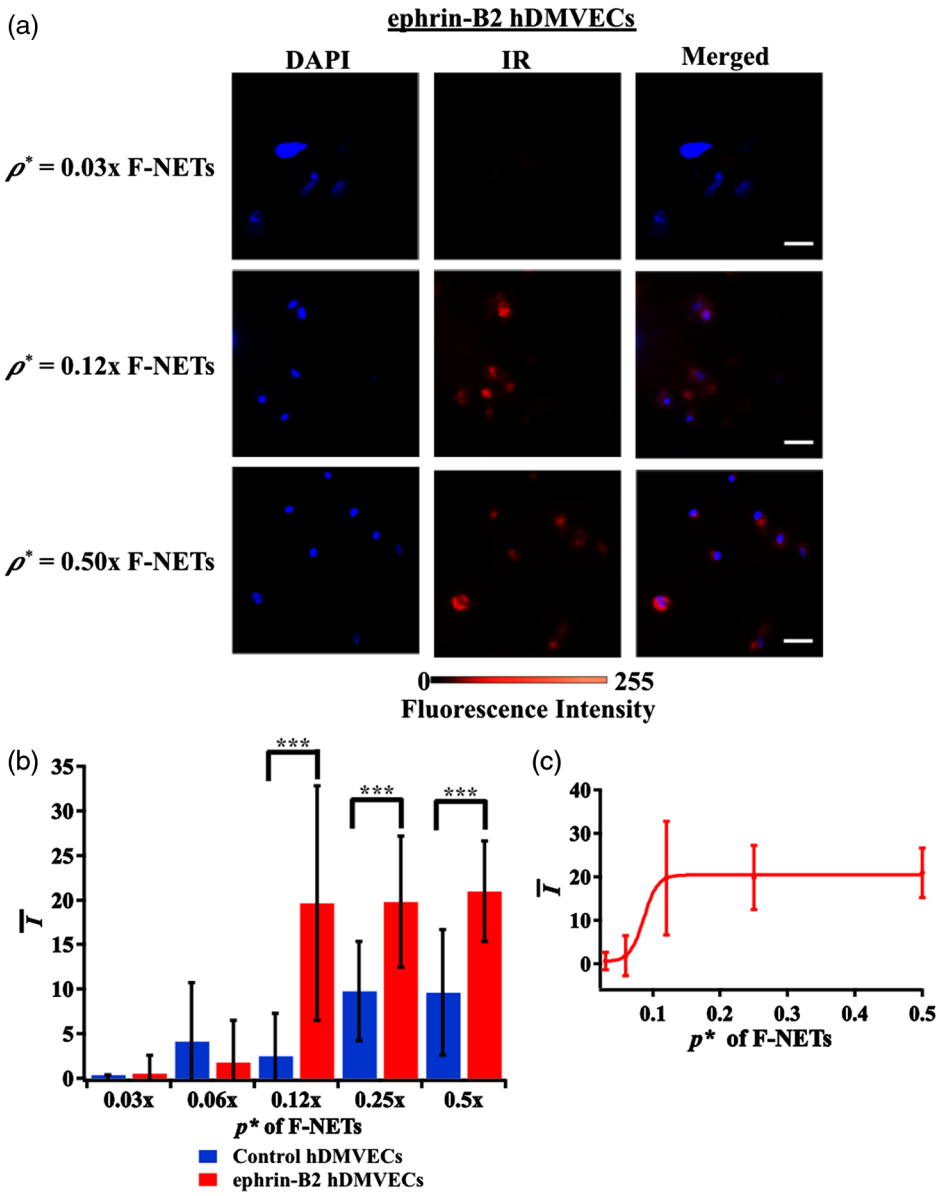

Fig. 7 Cellular fluorescence of control and ephrin-B2 hDMVECs incubated with F-NETs at various $\rho*$ values. (a) Fluorescent images of control and ephbin-B2 hDMVECs after 40 min of incubation at 4°C with F-NETs solutions. All images are falsely colored with the blue and red corresponding to DAPI and ICG NIR emission from the NETs, respectively. Scale bars are 30 μm. (b) Averaged fluorescence intensity ($\bar{I}$) [see Eq. (3)] as a function of $\rho*$. Cells from 3 to 4 images were analyzed, resulting in 16 to 41 measurements for each combination of nanoparticles and cells. Statistical significance of $p < 0.001$ is denoted by ***. Only statistically significant populations with the same $\rho*$ value of F-NETs are indicated. (c) Sigmoidal fit to the $\bar{I}$ values of the ephrin-B2 hDMVECs versus the $\rho*$ value of F-NETs. Error bars in (b) and (c) represent SDs.

fluorescence imaging results suggest that the uptake of such functionalized NETs by ephrin-B2 expressing cells follows a sigmoidal function that depends on the relative number density of F-NETs in the incubating medium.

Disclosures

The authors do not have any conflicts of interest to declare.

Acknowledgments

This study was supported in parts by grants from the National Science Foundation (CBET-1509218 to B.A.) and the National Institute of Arthritis and Musculoskeletal and Skin Diseases (R01-AR068067 to B.A. and R01-AR073172 to W.T.). The model of CD47 in Figs. 1 and 2 were based off the DNA sequence from protein data base entry 2JJS and were modeled using the Chimera Program from the University of California, San Diego.

References

1. D. B. Nikolov, K. Xu, and J. P. Himanen, "Homotypic receptor-receptor interactions regulating Eph signaling," *Cell Adhes. Migr.* **8**(4), 360–365 (2014).
2. E. M. Lisabeth, G. Falivelli, and E. B. Pasquale, "Eph receptor signaling and ephrins," *Cold Spring Harb. Perspect. Biol.* **5**(9), a009159 (2013).

3. C. T. Blits-Huizinga et al., "Ephrins and their receptors: binding versus biology," *IUBMB Life* **56**(5), 257–265 (2004).
4. E. B. Pasquale, "The Eph family of receptors," *Curr. Opin. Cell Biol.* **9**(5), 608–615 (1997).
5. Eph Nomenclature Committee, "Unified nomenclature for Eph family receptors and their ligands, the ephrins," *Cell* **90**(3), 403–404 (1997).
6. J. Frisén, J. Holmberg, and M. Barbacid, "Ephrins and their Eph receptors: multitalented directors of embryonic development," *EMBO J.* **18**(19), 5159–5165 (1999).
7. K. Kullander and R. Klein, "Mechanisms and functions of Eph and ephrin signalling," *Nat. Rev. Mol. Cell Biol.* **3**(7), 475–486 (2002).
8. H. Surawska, P. C. Ma, and R. Salgia, "The role of ephrins and Eph receptors in cancer," *Cytokine Growth Factor Rev.* **15**(6), 419–433 (2004).
9. C. M. Edwards and G. R. Mundy, "Eph receptors and ephrin signaling pathways: a role in bone homeostasis," *Int. J. Med. Sci.* **5**(5), 263–272 (2008).
10. E. B. Pasquale, "Eph-ephrin bidirectional signaling in physiology and disease," *Cell* **133**(1), 38–52 (2008).
11. Y. Chen, A. K. Y. Fu, and N. Y. Ip, "Eph receptors at synapses: implications in neurodegenerative diseases," *Cell. Signalling* **24**(3), 606–611 (2012).
12. W. Tan et al., "Coexistence of Eph receptor B1 and ephrin B2 in port-wine stain endothelial progenitor cells contributes to clinicopathological vasculature dilatation," *Br. J. Dermatol.* **177**, 1601–1611 (2017).
13. S. J. Riedl and E. B. Pasquale, "Targeting the Eph system with peptides and peptide conjugates," *Curr. Drug Targets* **16**(10), 1031–1047 (2015).
14. Z. Wang et al., "Specific photothermal therapy to the tumors with high EphB4 receptor expression," *Biomaterials* **68**, 32–41 (2015).
15. K. S. Blevins et al., "EphA2 targeting peptide tethered bioreducible poly(cystamine bisacrylamide–diamino hexane) for the delivery of therapeutic pCMV-RAE-1γ to pancreatic islets," *J. Controlled Release* **158**(1), 115–122 (2012).
16. A. M. Gobin, J. J. Moon, and J. L. West, "EphrinAl-targeted nanoshells for photothermal ablation of prostate cancer cells," *Int. J. Nanomed.* **3**(3), 351–358 (2008).
17. J. D. Obayemi et al., "Adhesion of ligand-conjugated biosynthesized magnetite nanoparticles to triple negative breast cancer cells," *J. Mech. Behav. Biomed. Mater.* **68**, 276–286 (2017).
18. K. Zhang et al., "Comprehensive optimization of a single-chain variable domain antibody fragment as a targeting ligand for a cytotoxic nanoparticle," *MAbs* **7**(1), 42–52 (2014).
19. A. M. Alkilany et al., "Homing peptide-conjugated gold nanorods: the effect of amino acid sequence display on nanorod uptake and cellular proliferation," *Bioconjug. Chem.* **25**(6), 1162–1171 (2014).
20. A. Barquilla and E. B. Pasquale, "Eph receptors and ephrins: therapeutic opportunities," *Annu. Rev. Pharmacol. Toxicol.* **55**, 465–487 (2015).
21. C.-M. J. Hu et al., "Erythrocyte membrane-camouflaged polymeric nanoparticles as a biomimetic delivery platform," *Proc. Natl. Acad. Sci. U. S. A.* **108**(27), 10980–10985 (2011).
22. B. Bahmani, D. Bacon, and B. Anvari, "Erythrocyte-derived phototheranostic agents: hybrid nano-vesicles containing indocyanine green for near infrared imaging and therapeutic applications," *Sci. Rep.* **3**, 2180 (2013).
23. J. T. Mac et al., "Erythrocyte-derived nano-probes functionalized with antibodies for targeted near infrared fluorescence imaging of cancer cells," *Biomed. Opt. Express* **7**(4), 1311–1322 (2016).
24. R. Vankayala et al., "Erythrocyte-derived nanoparticles as a theranostic agent for near-infrared fluorescence imaging and thrombolysis of blood clots," *Macromol. Biosci.* **18**, e1700379 (2018).
25. Y. Guo et al., "Erythrocyte membrane-enveloped polymeric nanoparticles as nanovaccine for induction of antitumor immunity against melanoma," *ACS Nano* **9**(7), 6918–6933 (2015).
26. R. H. Fang, C.-M. J. Hu, and L. Zhang, "Nanoparticles disguised as red blood cells to evade the immune system," *Expert Opin. Biol. Ther.* **12**(4), 385–389 (2012).
27. R. Li et al., "Cell membrane-based nanoparticles: a new biomimetic platform for tumor diagnosis and treatment," *Acta Pharm. Sin. B* **8**(1), 14–22 (2018).
28. J.-M. Liu et al., "Erythrocyte membrane bioinspired near-infrared persistent luminescence nanocarriers for in vivo long-circulating bioimaging and drug delivery," *Biomaterials* **165**, 39–47 (2018).
29. X. Wan et al., "Red blood cell-derived nanovesicles for safe and efficient macrophage-targeted drug delivery in vivo," *Biomater. Sci.* **7**, 187–195 (2018).
30. Q. Zhang et al., "Neutrophil membrane-coated nanoparticles inhibit synovial inflammation and alleviate joint damage in inflammatory arthritis," *Nat. Nanotechnol.* **13**(12), 1182–1190 (2018).
31. J. Li et al., "Cell membrane coated semiconducting polymer nanoparticles for enhanced multimodal cancer phototheranostics," *ACS Nano* **12**(8), 8520–8530 (2018).
32. C.-M. J. Hu, R. H. Fang, and L. Zhang, "Erythrocyte-inspired delivery systems," *Adv. Healthc. Mater.* **1**(5), 537–547 (2012).
33. J.-W. Yoo et al., "Bio-inspired, bioengineered and biomimetic drug delivery carriers," *Nat. Rev. Drug Discov.* **10**(7), 521–535 (2011).
34. A. A. Bentley and J. C. Adams, "The evolution of thrombospondins and their ligand-binding activities," *Mol. Biol. Evol.* **27**(9), 2187–2197 (2010).
35. P. A. Oldenborg et al., "Role of CD47 as a marker of self on red blood cells," *Science* **288**(5473), 2051–2054 (2000).
36. P.-A. Oldenborg, "CD47: a cell surface glycoprotein which regulates multiple functions of hematopoietic cells in health and disease," *ISRN Hematol.* **2013**, 1–19 (2013).
37. P. L. Rodriguez et al., "Minimal 'self' peptides that inhibit phagocytic clearance and enhance delivery of nanoparticles," *Science* **339**(6122), 971–975 (2013).
38. H. Zhang, "Erythrocytes in nanomedicine: an optimal blend of natural and synthetic materials," *Biomater. Sci.* **4**(7), 1024–1031 (2016).
39. J. M. Burns et al., "Erythrocyte-derived theranostic nanoplatforms for near infrared fluorescence imaging and photodestruction of tumors," *ACS Appl. Mater. Interfaces* **10**(33), 27621–27630 (2018).
40. C. Minelli and A. G. Shard, "Chemical measurements of polyethylene glycol shells on gold nanoparticles in the presence of aggregation," *Biointerphases* **11**(4), 04B306 (2016).
41. J. M. Burns et al., "Optical properties of biomimetic probes engineered from erythrocytes," *Nanotechnology* **28**(3), 035101 (2017).
42. J. C. Tang, A. Partono, and B. Anvari, "Near-infrared-fluorescent erythrocyte-mimicking particles: physical and optical characteristics," *IEEE Trans. Biomed. Eng.* **66**(4), 1034–1044 (2018).
43. J. E. Noble and M. J. A. Bailey, "Quantitation of protein," in *Methods in Enzymology*, R. R. Burgess and M. P. Deutscher, Eds., Vol. **463**, pp. 73–95, Academic Press, Amsterdam (2009).
44. N. Baumgarth and M. Roederer, "A practical approach to multicolor flow cytometry for immunophenotyping," *J. Immunol. Methods* **243**(1), 77–97 (2000).
45. D. A. Bryant, "Phycoerythrocyanin and phycoerythrin: properties and occurrence in cyanobacteria," *Microbiology* **128**(4), 835–844 (1982).
46. S. Behzadi et al., "Cellular uptake of nanoparticles: journey inside the cell," *Chem. Soc. Rev.* **46**(14), 4218–4244 (2017).
47. J. K. Chen et al., "An overview of clinical and experimental treatment modalities for port wine stains," *J. Am. Acad. Dermatol.* **67**(2), 289–304.e29 (2012).
48. S. L. Jacques, "Optical properties of biological tissues: a review," *Phys. Med. Biol.* **58**(11), R37 (2013).
49. J. Burns et al., "Photothermal treatment of port-wine stains using erythrocyte-derived particles doped with indocyanine green: a theoretical study," *J. Biomed. Opt.* **23**, 121616 (2018).

Taylor Hanley is a PhD candidate in bioengineering at the University of California, Riverside, California, USA. She received her MS degree in bioengineering from the University of California, Riverside, California, and her BS degree in biochemistry from Harvey Mudd College, Claremont, California. Her research focuses on functionalizing erythrocyte-derived nanoparticles to target specific diseased cell states for their imaging or phototherapy, as well as investigating the immunogenicity of these nanoparticles.

Rong Yin is a postdoctoral fellow in the Department of Cell Biology and Anatomy at the University of South Carolina School of Medicine. She holds her PhD in dermatological science from the Forth Military Medical University, China, 2018. Her research interests include the development of novel nanoparticles for photodynamic therapy for patients with congenital vascular malformations.

Jenny T. Mac is a PhD candidate in biochemistry and molecular biology at the University of California, Riverside, California. She received her MS degree in biochemistry and molecular biology and BS degree in biochemistry from the University of California, Riverside, California. Her research focuses on erythrocyte-derived delivery systems for fluorescent imaging and phototherapeutics of cancer cells, as well as investigating the biodistribution of these particles.

Wenbin Tan is an associate professor at the University of South Carolina School of Medicine. He holds a PhD in neurobiology and neurophysiology from the University of California, Los Angeles, in 2008. His current research interests include the molecular pathogenesis of congenital vascular malformations and development of new treatments for these diseases.

Bahman Anvari is a professor in the Department of Bioengineering at University of California, Riverside. His research interests are in photomedicine with current focus on the engineering of delivery platforms for light-based theranostics. He is a fellow of the American Association for the Advancement of Science (AAAS), the American Institute for Medical and Biological Engineering (AIMBE), the Biomedical Engineering Society (BMES), and SPIE.